Marine diagenesis of tephra aided the Palaeocene-Eocene Thermal Maximum termination

Jack Longman[a,b,c *], Thomas M. Gernon[c], Martin R. Palmer[c], Morgan T. Jones[d], Ella W. Stokke[d], Henrik H. Svensen[d].

[a] Marine Isotope Geochemistry, Institute for Chemistry and Biology of the Marine Environment (ICBM), University of Oldenburg, D-26129 Oldenburg, Germany

[b] School of Geography and the Environment, University of Oxford, South Parks Road, Oxford, OX1 3QY, UK.

[c] School of Ocean and Earth Sciences, University of Southampton, Southampton SO14 3ZH, UK

[d] Centre for Earth Evolution and Dynamics (CEED), University of Oslo, P.O. Box 1028 Blindern, 0315 Oslo, Norway

[*]**Corresponding Author: Jack Longman.** Address: Marine Isotope Geochemistry, Institute for Chemistry and Biology of the Marine Environment (ICBM), University of Oldenburg, D-26129 Oldenburg, Germany. Email: jack.longman@uni-oldenburg.de, Telephone: (49) 441-798-3359

Highlights

- Numerous Palaeocene-Eocene Thermal Maximum (PETM)-age tephras contain authigenic carbonate.
- Authigenic carbonate formed as a result of marine silicate weathering and anaerobic oxidation of methane in tephra layers.
- Authigenesis likely occurred during the PETM and acted as a major sink of isotopically-light carbon.

- The volcanism thought to have initiated the PETM may too have helped terminate it.

Keywords

PETM, authigenic carbonate, carbon cycle, volcanism, climate change, tephra

Abstract

The Palaeocene-Eocene Thermal Maximum (PETM) was a period of intense global warming that began ~55.9 million years ago and lasted about 170,000 years. Various mechanisms have been proposed to cause this warming, including the emplacement of the North Atlantic Igneous Province (NAIP). Equally, many mechanisms have been invoked to explain sequestration of carbon from the ocean-atmosphere system necessary to promote the recovery to more temperate conditions. Here we propose that an important path for carbon sequestration was tied to NAIP volcanism through the precipitation of calcium carbonate ($CaCO_3$) cements within the tephra layers. These cements formed after the deposition and burial of tephra over a wide area of the North Atlantic Ocean during the late Palaeocene and early Eocene. We find strong evidence that authigenic $CaCO_3$ cements formed shortly after tephra deposition. Monte Carlo simulations suggest that this process may have been responsible for a quarter of the carbon sequestered during the PETM recovery phase, providing a major, but previously unconsidered sink of isotopically-light carbon, and one which may have persisted into the Eocene.

1 Introduction

The late Palaeocene and early Eocene were punctuated by several episodes of rapid global warming or hyperthermals (Westerhold et al., 2018), characterised by negative carbon isotope excursions (CIEs) in sedimentary strata. The largest and best studied of these, the Palaeocene-Eocene Thermal Maximum (PETM), involved 4–5 °C of land surface warming and an up to 9 °C rise in sea surface temperatures over a period of 170,000 years (Dunkley Jones et al., 2013; Storey et al., 2007), that started ~55.9 million years ago (Ma) (Charles et al., 2011; Westerhold et al., 2018). Volcanic and thermogenic degassing associated with the formation of the North Atlantic Igneous Province (NAIP) has been invoked as a potential trigger (Gutjahr et al., 2017; Svensen et al., 2004), as well as other processes including carbon release from methane hydrates (Dickens et al., 1995), permafrost (Deconto et al., 2012), other organic matter sources (Higgins and Schrag, 2006), and potenitally a bolide impact (Schaller et al., 2016). Volcanic activity occurred across the North Atlantic region during the end of the Palaeocene and the early Eocene (Roberts et al., 1984; Steinberger et al., 2018; Svensen et al., 2004), with the intrusion of approximately 6.6×10^6 km^3 of magma (Saunders, 2016). Massive explosive eruptions also resulted in tephra deposition across much of north-western Europe and the North Atlantic Ocean, with PETM-age tephra found as far as Austria, c.1,900 km away from the source area (Egger and Brückl, 2006; Larsen et al., 2003; Stokke et al., 2020a) (Fig. 1). Importantly, coupled sea surface pH reconstructions and carbon isotope modelling indicate that the 3,000 Pg to >10,000 Pg of carbon emissions was required to initiate the PETM most likely derived from a volcanic source (Gutjahr et al., 2017). Other modelling results are consistent with regular injections of magmatic carbon over the ~50 kyr following its inception (Frieling et al., 2016), possibly linked to thermogenic degassing (Svensen et al., 2004).

The processes and feedbacks responsible for returning the ocean-atmosphere carbon system and global climate to pre-PETM conditions are debated. The drawdown of atmospheric CO_2 during the PETM recovery likely occurred more rapidly than can be attributed to silicate weathering alone (Bowen and Zachos, 2010), with evidence suggesting enhanced weathering also led to elevated organic carbon (C_{org}) burial (Bowen, 2013; Bowen and Zachos, 2010; Gutjahr et al., 2017). It has been suggested this may have occurred via an enhanced biological pump (Ma et al., 2014), amplified carbonate formation (Kelly et al., 2010, 2005), a deepening of the carbonate compensation depth (Penman et al., 2016), or a shift in the style of calcification (Boudreau et al., 2018). Thus, recent modelling studies have concluded that both enhanced silicate weathering feedbacks and greater levels of C_{org} burial drove the PETM recovery (Gutjahr et al., 2017; Penman and Zachos, 2018).

We suggest that tephra alteration on the seafloor during early burial and diagenesis may also have perturbed the carbon cycle. On decadal timescales, tephra may augment organic carbon (C_{org}) production in the vicinity of an eruption as nutrient-rich tephra alleviates phytoplankton nutrient deficiencies (particularly dissolved Fe), as observed for example, in the aftermath of the 2010 Eyjafjallajökull eruption (Achterberg et al., 2013), and in the northeast Pacific after the eruption of Kasatochi (Hamme et al., 2010). This is due to the rapid release of metal salts from tephra upon deposition in seawater (Jones and Gislason, 2008). Volcanism can also enhance C_{org} preservation via the isolation of organic matter from oxidants (Hembury et al., 2012) and the formation of stable organometallic complexes (Longman et al., 2019). During periods of extensive volcanism, authigenic carbonate (C_{auth}) may also form within widespread tephra blankets (Schrag et al., 2013; Wallmann et al., 2008). C_{auth} is largely derived from elevated pore water carbonate concentrations formed from methanogenesis and the anaerobic oxidation of methane (AOM) (Schrag et al., 2013), and thus sequesters organic carbon.

We investigated the potential impact of C_{auth} formation in PETM-age tephra deposits from the island of Fur, Denmark (Supplementary Figure 1), the Rockall Plateau (Deep Sea Drilling Project (DSDP) Leg 81, Holes 553A and 555), and a hydrothermal vent complex in the Vøring Basin offshore Norway (core 6607/12-1) (Fig. 1). The Rockall tephra layers were deposited immediately above basaltic lavas formed during the main phase (phase 2) of NAIP activity (see Methods) during the Paleogene (Roberts et al., 1984), the same activity that led to the deposition of the Fur tephras, which are preserved across Denmark (Larsen et al., 2003) and broadly coeval with hydrothermal vent formation (Frieling et al., 2016; Svensen et al., 2003) (Fig. 1).

2 Methods and Materials

2.1 Site Description

Holes 553A (56°05.32'N, 23°20.61'W, water depth 2339 m) and 555 (56°33.70'N, 23°46.93'W, water depth 1669 m) were drilled as part of DSDP Leg 81, in the north-eastern North Atlantic, with Hole 553A located to the edge of the Rockall Plateau, and Hole 555 on the plateau's western flank (Fig. 1). We also investigated samples from the Fur formation, Fur Island, Denmark (sampled at 56°50'15"N 8°57'36"E) (layers -33, -19, +22, +62, +82, +90, +94, +101, +102, +110 and +118; (Bøggild, 1918)), deposited during the latest Palaeocene and early Eocene (Larsen et al., 2003) (Fig. 1).

2.2 Geochemical Analyses

For the samples from Holes 553A and 555, inorganic ($CaCO_3$) carbon was measured on 20 mg of homogenised freeze-dried sediment via coulometry, with measurements made on evolved CO_2 resulting from acidification. A carbonate standard and an in-house stream sediment standard were analysed alongside samples to ensure accurate and repeatable

measurements. The same sample then underwent multiple rinses with Mili-Q water prior to drying. From this, a subsample (5 – 15 mg) was taken and organic carbon, sulfur and nitrogen content measured via a Vario PYRO cube elemental analyser coupled with a vision isotope ratio mass spectrometer (IRMS) at the University of Southampton. Bulk sediment carbon isotope signatures ($\delta^{13}C_{Bulk}$) were measured on the same evolved CO_2, and calibrated to USGS 40 and USGS 41a, with reproducibility of ±0.11 ‰, and ±0.06 ‰, respectively.

Using the coulometry results, samples from Sites 553A and 555 containing $CaCO_3$ were selected and analysed via a Thermo Scientific Kiel IV Carbonate device coupled to a MAT253 IRMS at the University of Southampton. Perchloric acid was applied to the bulk sediment, releasing CO_2, from which carbon and oxygen isotope values ($\delta^{13}C_{Carb}$ and $\delta^{18}O$) were obtained for the carbonate fraction. Replicate analyses of an in-house standard were calibrated to NBS-18 and NBS-19, with reproducibility of ±0.13 ‰ and ±0.12 ‰ respectively for $\delta^{13}C$, and ±0.17 ‰ and ±0.23 ‰ respectively for $\delta^{18}O$.

Tephra samples from Fur Island were dried and crushed prior to initial characterisation via an elemental analyser to infer carbonate content. Samples which contained >1% carbonate (layers +94, +101 and +102) were digested in phosphoric acid at 25°C prior to analysis of purified CO_2 on a VG SIRA 12 gas-source mass spectrometer at the University of Liverpool. NBS-19 was used as a reference standard, and average precision was between 0.1 ‰ for both carbon and oxygen. All isotope data are presented in delta notation, the per mil variation from the VPD Belemnite. Resolution of analyses depended upon sample availability, with DSDP samples taken at 5 cm resolution wherever possible, and single samples taken from each analysed tephra layer at Fur.

To determine the source of the volcanic material, the neodymium (Nd) isotope signal of several homogenised and freeze-dried tephra and hyaloclastite samples was investigated. After leaching in 6M HCl for 2 hours to remove any post deposition alteration-related

material, samples were dissolved using a mixed acid HNO_3-HF approach. The Nd-containing aliquot was purified via cation (AG50-X8 200-400 mesh resin) and reverse phase (LN Spec, Eichrom Industries) chromatography. Measurements were made using a Thermo Fisher Neptune MC-ICP-MS at the University of Southampton.

2.3 Calculations and Modelling

We used existing isopach maps developed from tephra thickness measurements across the North Atlantic region to estimate the area covered by tephra during the PETM (Egger and Brückl, 2006; Obst et al., 2015). These isopachs were produced from mapped outcrops of Fur tephra layer +19, which has been correlated to sediments from DSDP Site 550 (Goban Spur) and the Austrian Alps (Egger and Brückl, 2006). By using the isopachs of this tephra layer, its known thickness at Fur, and by assuming a common source of all tephra layers, isopachs of all PETM-age tephras deposited in the Fur formation were developed (Supplementary Table 1, Fig. 1). This method calculates the thickness of each tephra at each outcrop as a proportion of tephra layer +19, using tephra thicknesses measured at Fur. For example, tephra layer +19 is 19 cm thick at Fur, and 2.5 cm thick in Hole 550 (Egger and Brückl, 2006). Using the proportional relationship between the tephra extents, tephra layer -33 (deposited at the transition between the main body and recovery phase of the PETM carbon isotope excursion (Egger and Brückl, 2006)) is 20 cm thick at Fur, and so we calculate it to be 2.6 cm thick in DSDP Site 550. We use this approach to estimate the volume of each tephra layer present at Fur (Supplementary Table 1). For each tephra layer, therefore, we produce an estimate of its thickness in each outcrop of PETM-age tephra (Supplementary Table 1). To convert tephra thicknesses and isopach estimates to tephra volumes, the Weibull interpolation method was used (Bonadonna and Costa, 2012). This approach fits a Weibull distribution to a graph of the square root of isopach area against tephra thickness. For each tephra layer, values for θ (a thickness scale), λ (the decay length scale of deposit thinning) and n (a

dimensionless shape parameter) were optimised to attain the best Weibull fit. This optimisation was completed using the Solver function in Microsoft Excel to fit the Weibull distribution curve most closely to the data before integration to attain an estimate of tephra volume for each layer. By comparing observed tephra layer thicknesses to those developed by the Weibull fit, difference values and mean absolute percentage errors (MAPE) were developed (Supplementary Table 1). These estimates of tephra deposition were then summed to attain some estimates of the total volume of tephra deposited during the PETM, and are in line with previous estimates of tephra transport (Egger and Brückl, 2006; Stokke et al., 2020b).

To estimate the impact of C_{auth} formation in hydrothermal vent structures, estimates of the number (N_{vent}), radius (R_{vent}) and depth (D_{vent}) of such structures were used (Frieling et al., 2016; Planke et al., 2005; Svensen et al., 2003). Using these values, we estimated the volume of tephra filling these vents. For both the tephra layers and vent structures, estimated tephra volumes (V_T, in km^3), and measured percentages of $CaCO_3$ (C_{carb}) were then used to calculate the volume of carbonate (V_{carb}, in m^3). From this value, the total weight of carbonate in the tephra (W_T, in kg) was calculated using the density of carbonate (D_{carb}, 2711 kg/m^3, Eq. 1).

$$W_T = V_{carb} \times D_{carb} \quad \text{(Eq. 1)}$$

As several variables contribute to the final amount of sequestered carbon in both tephra layers and vent structures, a probabilistic modelling approach (cf. Gernon et al., 2016) was used. Repeat Monte Carlo simulations were employed to develop values for each of the variables in both the tephra layers (V_T, C_{carb}) and vent structures (N_{vent}, R_{vent}, D_{vent} and V_T) from plausible ranges (Supplementary Tables 2, 3). The derived ranges are related to uncertainties (e.g., in the number, size and depth of vent structures), variability arising from different methods used (e.g., V_T), or from observed variability (e.g., C_{carb}). Each iteration uses values developed for each of the variables, and so by modelling repeatedly, most likely outcomes are simulated.

For all variables, 10,000 simulations were run using the R package *truncnorm* and the function *rtruncnorm*, which produced 10,000 random datapoints between specified boundaries. Using standard deviations and means (Supplementary Tables 2, 3), a Gaussian distribution between the boundaries was developed. Any simulations that fell outside of the boundaries were resampled, ensuring realistic ranges were developed, and unrealistic data (e.g., C_{Carb} values below 0) avoided. For V_T, these simulations were developed from the sum of all tephra layers. Standard deviations were developed using mean absolute percentage error (MAPE) values, with an additional 25% error to account for the uncertainty in isopach measurements[15]. The lower boundary of models was determined using the absolute value of this error, and the upper boundary was left at infinity (Supplementary Table 2). This is because the uppermost volume estimates are likely to be underestimates, as PETM-age tephras have been located in localities even more distal than Austria (e.g., the Polish Carpathians (Obst et al., 2015)), and not all distal deposition has been considered in the isopach construction. For C_{Carb}, average and standard deviation values were determined from data presented here. Boundaries on these simulations were placed at 0.01% (because all tephra layers contain some $CaCO_3$) and at 50% (because 50% is the upper porosity value recorded in the tephras).

As the simulations for tephra layers do not discriminate between tephra settling onto land (where diagenetic reactions would not occur, or occur very slowly) and the ocean, we also estimated the amount of tephra falling into the ocean at the time of interest. We measured the land coverage of each of the isopachs (Egger and Brückl, 2006) used in these models (Fig. 1), and then assumed a 20% error in measurement to derive standard deviations and boundaries (Supplementary Table 2). From this range, 10,000 possible iterations for the fraction falling into the ocean were developed, and these fractions were used to multiply through the output sequestration values.

We use the following mass balance equation to assess the isotopic shift associated with the removal of carbon through C_{auth} formation (Eqs. 2-3):

$$\delta^{13}C\ after\ PETM\ (F) = \delta^{13}C\ during\ PETM(O) - \delta^{13}C\ removed\ via\ C_{auth}\ formation(A) \quad \text{(Eq. 2)}$$

$$\delta^{13}C_F M_F = \delta^{13}C_O M_O - \delta^{13}C_A M_A \quad \text{(Eq. 3)}$$

Where M is the mass of carbon. We use a value of 50,000 Pg as the active carbon pool both during and after the PETM (i.e., M_F and M_A). We use a nominal value of -1‰ for $\delta^{13}C_O$. We use a Monte Carlo modelling approach to provide a range of estimates for the other variables. For $\delta^{13}C_A$ we use the average and standard deviation of all analyses presented in Figure 3. For M_A we use the output of the previous Monte Carlo modelling of sequestration values. To compare to previous estimates, we run a similar set of Monte Carlo simulations of sequestration via organic carbon (C_{org}) formation. For this, we use the C_{org} isotope value of -30.5‰ (Gutjahr et al., 2017), and the carbon sequestration estimate of 2000 Pg C (Ma et al., 2014). To account for error in these numbers, we apply a standard deviation of 20% to the values prior to Monte Carlo modelling.

2.4 DSDP core chronologies

The stratigraphic sections of interest (Site 553A Cores 35 – 37, Site 555 Cores 56 – 69, and selected tephra layers below these sections in Site 555) were deposited immediately above basaltic lavas formed at the late Palaeocene, the same activity which led to the deposition of the Fur tephra layers (Larsen et al., 2003). We provide a detailed discussion of their stratigraphic ages in the Supplementary Materials.

3 Results and Discussion

3.1 Evidence for widespread C_{auth} formation

The Rockall tephra layers typically comprise 2–15 wt% $CaCO_3$ infilling porosity (Fig. 2, Figs. 3,4), but locally as high as 50 wt% (Fig. 3a). By comparison, the $CaCO_3$ contents are near-zero in the mudstones that host the Rockall tephras (Fig. 2, Supplementary Fig. 2). The Fur tephra layers show a bimodal distribution of $CaCO_3$ cements, with eight containing 0.4–1% and three containing 40–50% (Supplementary Table 4).

Carbonate cements have been documented in many early Eocene tephra layers, with concretions comprising up to 52% $CaCO_3$ reported from the Mo-clay (Denmark) (Pedersen and Buchardt, 1996). Further examples are reported in coeval tephras in northern Germany (Obst et al., 2015), the North Sea basin (Morton and Knox, 1990), the northern North Sea and eastern England (Haaland et al., 2000). Tephras of this age from the North Sea basin comprise the Sele and Balder formations, with the Sele formation correlated to late Palaeocene and early Eocene tephras at Fur and across the North Sea (Knox, 1997; Morton and Knox, 1990), and related to Phase 2 of NAIP volcanism. The PETM interval, as observed in the Sele formation from the Grane field (Jones et al., 2019), contains numerous tephra-rich layers, with 5 – 30 wt% calcite cements in these layers (Haaland et al., 2000). In addition, carbonate cements (Fig. 4) occur within tephras hosted by Eocene diatomites above a hydrothermal vent complex, which formed as a result of the explosive release of volatiles generated by sill intrusions into organic-rich sediments (Frieling et al., 2016; Svensen et al., 2003, 2004). This vent complex is thought to have formed during the PETM (Svensen et al., 2004), and the associated carbonate cements—which are Eocene in age (Frieling et al., 2016)—exhibit an organic carbon $\delta^{13}C$ signature (Frieling et al., 2016; Svensen et al., 2004, 2003).

3.2 Modes of C_{auth} formation

C_{auth} forms when the pore water concentrations of carbonate and/or divalent cations exceed the saturation index of a carbonate mineral, and the kinetic barrier associated with the formation of the specific mineral is breached. This typically occurs at sub-seafloor depths >1 m, which are coincident with high alkalinity—a result of sulfate reduction and AOM (Schrag et al., 2013), and the decomposition of organic carbon. Within tephra layers, much of the Ca^{2+} is derived from the alteration of volcanic material (Hong et al., 2020), in a similar manner to the process that drives $CaCO_3$ precipitation in the oceanic crust (Alt and Teagle, 1999). However, we cannot rule out other sources of calcium such as seawater and migrating pore fluids. When tephra is deposited, it rapidly takes up dissolved oxygen, leading to the depletion to zero of pore water O_2 within as little as 2.5 mm of the sediment-water interface (Hembury et al., 2012) (Supplementary Fig. 3). Simultaneously, there is a small decrease in the pH of marine sediment pore water directly below tephra (Homoky et al., 2011) (Supplementary Fig. 3). Deposition of as little as 5 cm of tephra is sufficient to isolate underlying sediments from O_2 exposure, resulting in low levels of C_{org} oxidation, and consequently high levels of organic matter preservation (Hartnett et al., 1998; Hembury et al., 2012).

The isotopic composition of carbonates provides insights into their origin. Carbon isotopes from the carbonate fraction ($\delta^{13}C_{Carb}$) of tephras from Site 553A range from -4.72 to -17.61 ‰, with a mean of -13.95 ‰ (n= 22), overlapping with the range observed in the Fur tephras (-13.89 to -26.95 ‰, n=3) (Supplementary Table 4). The $\delta^{13}C_{Carb}$ signatures are comparable to those of diagenetic carbonates reported within Eocene-age tephras (Fig. 3). The ^{13}C-depleted nature of these cements attests to the incorporation of light, AOM and methanogenesis-derived carbon acting on the C_{org}-rich sediments as they are buried to below the sulfate reduction zone (Schrag et al., 2013; Whiticar and Faber, 1986). These processes

lead to the upward diffusion of methane, with AOM occurring where methane reaches pore waters containing dissolved sulfate (Sivan et al., 2007). Alternatively, in the environments considered here (given the active nature of local volcanism) the methane may derive from thermal metamorphism of organic-rich sedimentary rocks by intruding magma (Frieling et al., 2016; Svensen et al., 2004) (Fig. 5).

C_{auth} formation accounts for between 0.1 and 1% of carbonate accumulation in modern, oxygen-rich oceans[41], but during periods of low atmospheric oxygen and widespread ocean anoxia, the C_{auth} sink may have been a much more important part of the carbon cycle (Longman et al., 2019; Schrag et al., 2013). Due to the reductive nature of reactive Fe phases in the tephras (Supplementary Figure 3), the diagenetic environment within and below these layers was likely anoxic (Haeckel et al., 2001; Hembury et al., 2012). In anoxic C_{org}-rich sediments, decomposition of the organic fraction occurs via two mechanisms as the sediment moves through the zone of sulfate reduction during burial: particulate organic carbon sulfate reduction (POCSR, eq. 4) and methanogenesis (ME, eq. 5).

$$POCSR: 2(CH_2O)_x(NH_3)_y(H_3PO_4)_z + SO_4^{2-} \rightarrow xH_2S + 2xHCO_3^- + 2yNH_3 + 2zH_3PO_4$$

(Eq.4)

$$ME: 2(CH_2O)_x(NH_3)_y(H_3PO_4)_z \rightarrow xCH_4 + xCO_2 + 2yNH_3 + 2zH_3PO_4 \text{ (Eq.5)}$$

Where x, y and z are the generalised number of C, N and P atoms. In marine C_{org}, this is typically assumed to reflect the Redfield ratio (C:N:P=106:16:1). As the sediment reaches the sulfate-methane transition zone, further C_{org} breakdown occurs via the anaerobic oxidation of methane (AOM, eq. 6):

$$AOM: CH_4 + SO_4^{2-} \rightarrow HS^- + HCO_3^- + H_2O \text{ (Eq.6)}$$

In both POCSR and AOM sulfate ions act as the electron accepter. Background sediments at Rockall are C_{org} rich (1.5 – 2 wt% C_{org}; Fig. 2), and are sufficient to saturate pore fluid with

ME-derived CH_4 (Kim et al., 2016; Pohlman et al., 2009). All three degradation processes lead to the formation of bicarbonate ions, with CO_2 a product of ME. Released HCO_3^- ions may combine with Ca^{2+} or Mg^{2+} from seawater or tephra alteration to form carbonate (Eq.7):

$$Carbonate\ formation: Ca^{2+} + HCO_3^- \rightarrow CaCO_3 + H^+ \quad \text{(Eq.7)}$$

However, in a typical anoxic marine sedimentary environment, the CO_2 released by ME would lower pH to the point where carbonate is dissolved rather than precipitated (Kim et al., 2016; Sample et al., 2017; Torres et al., 2020). Stoichiometrically, the reactions described in equations 1 and 2 would not release sufficient HCO_3^- to offset the CO_2-related acidity increase (i.e., via its transformation to carbonic acid), and so solid carbonate will not be saturated, and will instead dissolve (Torres et al., 2020). In the studied deposits at Rockall, this is clearly not the case as carbonates have precipitated in all tephras (Fig. 2). In anoxic marine sediments containing high levels of reactive silicate minerals (Hong et al., 2020), such as those which are tephra-rich in this study, CO_2 released from ME also drives marine silicate weathering (MSiW). This, in a generalised form, is the breakdown of silicates by CO_2 and H_2O (Eq. 8), a process which results in the formation of carbonates due to the release of divalent cations and bicarbonate ions (Solomon et al., 2014; Wallmann et al., 2008).

$$MSiW: Cation\ Rich\ Silicates + CO_2 + nH_2O \rightarrow Cation\ Poor\ Silicates + HCO_3^- + H_4SiO_4 + Ca^{2+} + Other\ Dissolved\ Cations \quad \text{(Eq.8)}$$

This process also raises alkalinity, effectively buffering pore water pH, and keeping dissolved carbonate in the bicarbonate form, leading to C_{auth} precipitation (Kim et al., 2016; Solomon et al., 2014). The ^{13}C-depleted nature of the carbonates studied here attests to their formation via methanogenesis, and the occurrence of C_{auth} solely within the tephra indicates that MSiW has enhanced carbonate preservation in these layers (Figs. 2, 3). However, the C_{auth} $\delta^{13}C$ values are not close to what would be considered a pure CH_4 signature (i.e., approximately -

60‰; Whiticar and Faber, (1986)), indicating that MSiW-derived bicarbonate ions, containing heavier carbon derived from ME, are also incorporated in the C_{auth}. In the background sediment, outside the tephra layers, CO_2 from ME likely decreased pH to the point where dissolution occurred, with no MSiW to consume the excess protons.

Modelling indicates that in anoxic locations of MSiW, the calcite (and dolomite) saturation state never falls below zero, with C_{auth} potentially precipitated in the first few thousand years after burial to the zone of sulfate reduction (Torres et al., 2020). This speed of formation is supported by measurements of burial speed and C_{auth} formation in the Sea of Okhotsk, where the shallow seas and organic-rich conditions are analogous to the proto-North Atlantic. Here, burial to the AOM depth typically takes ~5–50 kyr (Wallmann et al., 2008), ~3 m below the seafloor (Wallmann et al., 2006). Accordingly, with sedimentation rates at Fur ~60 mm/kyr (i.e., 60 m deposition in 1 Myr; Stokke et al., 2020b), this burial would take ca. 50 kyr. Therefore, extensive C_{auth} formation in tephra layers most likely occurred during the PETM initiation and recovery period (Fig. 5).

In environments such as those found within the tephra layers studied here, silicate weathering facilitated C_{auth} precipitation, and prevented the return of CO_2 and CH_4 to the ocean-atmosphere system, thereby representing a carbon sink which offsets the effect of alkalinity sequestration (Torres et al., 2020). C_{auth} formation in anoxic sediments as a result of MSiW has been documented in modern oceans, typically in locations of high C_{org} burial and often at continental margins (Kim et al., 2016; Scholz et al., 2013; Solomon et al., 2014; Sun and Turchyn, 2014; Wallmann et al., 2008), and across the Arctic Ocean (März et al., 2015). Of particular interest to our study is the appearance of C_{auth} in sediments which have experienced MSiW of tephra, with examples from the Nankai Trough and the Sea of Okhotsk (Sample et al., 2017; Wallmann et al., 2008), and likely in the Bering Sea (Hein et al., 1979). The most recent estimate of the size of this sink in modern oceans place it at 1-4 × 10^{12} mol C yr^{-1}

(Sample et al., 2017), but this relies solely upon estimates of global methane flux and does not consider hotspots of C_{auth} precipitation (Wallmann et al., 2012), such as observed here in tephra layers. During the PETM, the emplacement of large amounts of tephra to the organic-rich proto-North Atlantic would have provided the ideal environment for large-scale C_{auth} formation, as evidenced by the widespread occurrence of C_{auth} in contemporaneous tephra layers (Figs. 2, 3). Further, it is possible the alteration of tephra and in particular the release of silicic acid during carbonate precipitation (Eq. 8), would have aided the supply of nutrients to phytoplankton (März et al., 2015), thereby forming a positive feedback loop, by stimulating productivity and increasing background sediment C_{org}, in turn increasing the availability of C_{org} for ME and POCSR.

In addition to C_{auth} formation in tephra layers, carbonate cap formation is thought to occur above hydrothermal vent systems, where it is precipitated within tephra-rich sediments (Frieling et al., 2016; Svensen et al., 2003). Here, methane release forms C_{auth} deposits in diatomite ooze above the vent-fill, interpreted as sourced from methane seeping through permeability pathways related to vent formation. Some of these vents have been precisely dated to the PETM interval, but it is uncertain when the C_{auth} deposits formed (Frieling et al., 2016). As such, the diagenesis of vent-filling tephra may have played an extended role in C_{auth} formation throughout the early Eocene.

3.3 Modelling the potential impact of this tephra diagenesis

All the late Palaeocene and early Eocene-age tephra layers studied here have experienced some degree of early diagenetic alteration, and in most cases this has included C_{auth} formation. It has been suggested that the removal of ~2000 Pg C from the carbon cycle over a period of 30-40 kyr is required to drive the carbon isotope shift observed across the PETM recovery period (Bowen and Zachos, 2010; Gutjahr et al., 2017; Ma et al., 2014). To estimate the potential impact of C_{auth} formation on carbon sequestration, we used Monte Carlo

simulations to quantify the amount of carbon (via C_{auth} formation) consumed during alteration of the extensive tephra deposits just prior to, during and immediately following the PETM CIE (Supplementary Table 3). We define the period using Fur chronology, commencing at the start of the PETM (tephra layer SK1; Jones et al., (2019)) and ending with the final recovery back to pre-PETM conditions (Ash -21a) (Supplementary Fig. 1, Supplementary Table 1, Westerhold et al., (2009)). These estimates of tephra deposition were then summed to attain a value for total volume of tephra deposited during the PETM. This estimate of volume was combined with the measured range of C_{auth} formed in the tephras, a range of tephra densities, and an estimate of oceanic deposition (see Methods) to derive a value of carbon sequestration.

These simulations demonstrate the probability of tephra diagenesis playing a major role in carbon sequestration during the PETM and contributed to the return to pre-PETM climatic conditions. It is important to note, however, that these simulations suggest this process was not the sole reason behind the rapid recovery, but rather that it acted in concert with other processes to result in the rapid termination of the PETM – i.e., no single mechanism can be invoked to explain a complex interval of carbon cycle dynamics. The mean level of carbon sequestration in the tephras is on the order of 340 Pg C, just under a fifth of that necessary to enable full recovery (Fig. 6), whilst the upper end (95^{th} percentile) of the models correspond to roughly 850 Pg C, or 40% of the requisite sequestration.

Note that the modelled extent of tephra deposition is deliberately conservative (see Methods) and estimates of exceedance may better reflect the amount of C sequestration (Fig. 4B-C). The total amount of carbon sequestration is closely, but not exclusively, dependent on the amount of tephra deposited. For models reconstructing the volume of tephra as <10,000 km^3 (i.e., post-eruption volume), there is a 25% probability of exceeding 500 Pg C sequestration. This increases to 55% in models where the total erupted tephra volume is >20,000 km^3 (Fig.

4B). Evidence for the likelihood of extensive tephra deposition comes from observations that individual eruptions produced as much as 1,200 km^3 tephra (Egger and Brückl, 2006), and the total volume of material from Phase 2 of NAIP volcanism was as much as 6.6×10^6 km^3 . (Saunders, 2016, Fig. 6b). Furthermore, >1,000 Pg C sequestration is exceeded in 18% of models simulating eruptive tephra volumes exceeding 20,000 km^3.

We investigated the model dependency on $CaCO_3$ concentrations within the tephra layers and found that when an average of >10% $CaCO_3$ is formed, approximately 50% of our simulations indicate >500 Pg C sequestration (Fig. 6c). Furthermore, when an average $CaCO_3$ content of >30 wt% is formed, all our simulations result in sequestration of >500 Pg C, and 25% of the simulations result in sequestration of >1000 Pg C. Because observed $CaCO_3$ concentrations vary greatly in the studied sections, and previous work has documented both the formation of massive diagenetic carbonate deposits above hydrothermal vent complexes (Svensen et al., 2003), and very high carbonate cement abundances (e.g., comprising 5-30 wt% of Sele formation tephras; Haaland et al., 2000), high carbonate concentrations in the tephras are likely.

Overall, our models indicate tephra diagenesis most likely sequestered between 10–40% of the carbon necessary to terminate the PETM. Such levels are of a similar order of magnitude to other proposed mechanisms, with speculative calculations indicating ~2,000 Pg C sequestration over the 30–40 kyr of the PETM recovery via a more efficient biological pump (Ma et al., 2014), and 1,700 Pg C as a result of redox-controlled carbon-phosphorous feedbacks (Komar and Zeebe, 2017). These processes are not mutually exclusive, and it is considered likely that they combined with tephra diagenesis to prompt recovery from the PETM. Indeed, the close temporal correlation between the re-emergence of explosive volcanism and the PETM recovery (Jones et al., 2019; Stokke et al., 2020a, 2020b) suggest

tephra diagenesis may have acted as a final mode of carbon sequestration to terminate the hyperthermal.

To further assess the impact of this process on the carbon cycle in the Early Eocene, we carried out mass balance calculations in combination with the outputs of our Monte Carlo models (Methods). This approach allows us to investigate the potential role C_{auth} formation, and the sequestration of isotopically light carbon had on the carbon isotopic composition of Early Eocene sediments. This exercise indicates that C_{auth} formation from tephra diagenesis most likely resulted in a 0.2‰ shift, but with the uppermost estimate (95^{th} percentile) indicating up to 0.5‰ (Fig. 7). An additional, small shift from vent diagenesis is also calculated, with a mean value of 0.06‰, which rises to 0.3‰ in the 95^{th} percentile of models (Fig. 7). The average carbon isotope excursion associated with the PETM is -2.8‰ in marine archives (McInerney and Wing, 2011). Therefore, given a total carbon isotope shift of up to 0.8‰, C_{auth} formation may contribute to the return of seawater $\delta^{13}C$ values to pre-PETM values.

This is especially true when combined with the impact of postulated rapid C_{org} burial (Gutjahr et al., 2017). Taking an average isotopic signature of C_{org} to be -30.5‰ (Gutjahr et al., 2017), and an average 2000 Pg C sequestered (Ma et al., 2014), the isotopic shift associated with C_{org} burial is likely 1.2‰ (Fig. 7), increasing to 1.7‰ in the 95^{th} percentile of models (Fig. 6). It must be noted the value of 2000 Pg C is only sufficient to drive the carbon sequestration of the recovery period (Ma et al., 2014), and does not account for the total isotopic excursion, but it is clear that the addition of C_{auth} formation to the isotopic mass balance could contribute to the rapid recovery of the Earth system after the PETM. The process of enhanced C_{auth} formation during the PETM also helps explain the absence of a concurrent major C_{org} sink during this time (Dickson et al., 2014), and the observation that current carbon cycling

models are missing a sink of isotopically-light carbon (Komar and Zeebe, 2017; Penman and Zachos, 2018).

Our modelling only considers sequestration during the PETM, which comprises a small proportion of the total tephra deposited during the interval of NAIP activity. Hence, it is likely that similar processes continued to occur after the PETM. Further tephra layers were deposited regularly in the immediate aftermath of the PETM (Supplementary Fig. 1) and their diagenesis may have prompted sustained carbon sequestration across the NAIP, if we assume the diagenetic environment remained similar throughout the early Eocene. Indeed, this enduring carbon sink may account for the lack of large hyperthermal events between the PETM and Eocene Thermal Maximum 2 (ETM2, 53.7 Ma) despite continued eruptions from the NAIP (Larsen et al., 2003; Stokke et al., 2020a). Sediments from the 2 million year interval between the PETM and ETM2 contain abundant tephra deposits, particularly in the Fur formation where the extensive tephras of the "positive series" are recorded (Bøggild, 1918; Jones et al., 2019; Stokke et al., 2020a). A total of 140 tephra layers, some as thick as 18 cm, were deposited in the PETM aftermath (Supplementary Fig. 1), associated with large-scale explosive volcanism, combined with significant extrusive volcanism, which likely injected large quantities of CO_2 into the atmosphere (Stokke et al., 2020b). However, there is no evidence that these eruptions led to warming events, hence further C_{auth} formation in these tephra layers may have prevented the inception of further large-scale hyperthermals. Preliminary evidence of the cooling effect of tephra diagenesis through the early Eocene can be found in the sea surface temperature (SST) record from Fur (Stokke et al., 2020a), which shows an extended period of cooler SSTs in the North Atlantic following the PETM, echoed in estimates of bottom water temperature change (Vickers et al., 2020). The final layers of the "positive series" were deposited well before ETM2, so any C_{auth} sink would not have been active during its inception, thus allowing further hyperthermal initiation.

During the early Eocene, some vent structures (such as that considered here) are capped by C_{auth}-bearing sedimentary rocks (Frieling et al., 2016; Svensen et al., 2003), trapping methane and preventing further degassing to the atmosphere (Fig. 5). We quantified the potential impact of the diagenesis of vent-related tephras across the NAIP by constructing a similar Monte Carlo simulation (Supplementary Fig. 6, Supplementary Table 3). This yields a mean value of ~100 Pg C sequestered, with the 95^{th} percentile of simulations yielding ~400 Pg C (Supplementary Fig. 4), potentially adding another important carbon sequestration mechanism (Fig. 5) during the early Eocene. These results suggest that vents also played a role in suppressing hyperthermal inception prior to ETM2.

Overall, therefore, the clear temporal association between NAIP explosive volcanism and the termination of the PETM, coupled with the widespread volcanogenic carbon sequestration reported here, suggests that tephra diagenesis played an important role as a carbon sink from the ocean-atmosphere system during the terminal stages of the PETM, and in modulating the post-PETM climate.

Acknowledgements

This work was funded by Natural Environmental Research Council (NERC) grant, NE/K00543X/1. TG was supported by NERC grant, NE/R004978/1, and Turing Institute grant, EP/N510129/1. TG acknowledges the Distinguished Geologists Memorial Fund of the Geological Society of London to sample the Rockall tephras at the IODP Bremen Core Repository (BCR). We are thankful to the staff of the BCR, especially W. Hale, for their assistance, and to B. Hambach, M. Spencer, A. Michalik and A. Milton (University of Southampton), and S. Crowley (University of Liverpool) for laboratory assistance. Bo Schultz (Fur Museum, Denmark), Christian Tegner (Univ. Aarhus), and Sverre Planke (CEED) are thanked for field assistance. MTJ, EWS, and HHS were supported by the Research Council of Norway through its Centres of Excellence funding scheme, project

number 223272; while MTJ and EWS were also funded by the Research Council of Norway Unge Forskertalenter project “Ashlantic”, project number 263000.

Data Availability

Source data for Figs. 2 and 3, and Supplementary Fig. 2 have been made available in Supplementary Table 1. All other datasets generated during and/or analysed during the current study are available from the corresponding author on reasonable request.

4 References

Achterberg, E.P., Moore, C.M., Henson, S.A., Steigenberger, S., Stohl, A., Eckhardt, S., Avendano, L.C., Cassidy, M., Hembury, D., Klar, J.K., Lucas, M.I., Macey, A.I., Marsay, C.M., Ryan-Keogh, T.J., 2013. Natural iron fertilization by the Eyjafjallajökull volcanic eruption. Geophys. Res. Lett. 40, 921–926. https://doi.org/10.1002/grl.50221

Alt, J.C., Teagle, D.A.H., 1999. The uptake of carbon during alteration of ocean crust. Geochim. Cosmochim. Acta 63, 1527–1535. https://doi.org/10.1016/S0016-7037(99)00123-4

Bøggild, O.B., 1918. Den vulkanske Aske i Moleret samt en Oversigt over Danmarks ældre Tertiærbjergarter. Danmarks Geol. Undersøgelse, Raekke 2, 159.

Bonadonna, C., Costa, A., 2012. Estimating the volume of tephra deposits: A new simple strategy. Geology 40, 415–418. https://doi.org/10.1130/G32769.1

Boudreau, B.P., Middelburg, J.J., Luo, Y., 2018. The role of calcification in carbonate compensation. Nat. Geosci. 11, 894–900. https://doi.org/10.1038/s41561-018-0259-5

Bowen, G.J., 2013. Up in smoke: A role for organic carbon feedbacks in Paleogene hyperthermals. Glob. Planet. Change 109, 18–29.

https://doi.org/10.1016/J.GLOPLACHA.2013.07.001

Bowen, G.J., Zachos, J.C., 2010. Rapid carbon sequestration at the termination of the Palaeocene-Eocene Thermal Maximum. Nat. Geosci. 3, 866–869. https://doi.org/10.1038/ngeo1014

Charles, A.J., Condon, D.J., Harding, I.C., Pälike, H., Marshall, J.E.A., Cui, Y., Kump, L., Croudace, I.W., 2011. Constraints on the numerical age of the Paleocene-Eocene boundary. Geochemistry, Geophys. Geosystems 12, n/a-n/a. https://doi.org/10.1029/2010GC003426

Deconto, R.M., Galeotti, S., Pagani, M., Tracy, D., Schaefer, K., Zhang, T., Pollard, D., Beerling, D.J., 2012. Past extreme warming events linked to massive carbon release from thawing permafrost. Nature 484, 87–91. https://doi.org/10.1038/nature10929

Dickens, G.R., O'Neil, J.R., Rea, D.K., Owen, R.M., 1995. Dissociation of oceanic methane hydrate as a cause of the carbon isotope excursion at the end of the Paleocene. Paleoceanography 10, 965–971. https://doi.org/10.1029/95PA02087

Dickson, A.J., Rees-Owen, R.L., März, C., Coe, A.L., Cohen, A.S., Pancost, R.D., Taylor, K., Shcherbinina, E., 2014. The spread of marine anoxia on the northern Tethys margin during the Paleocene-Eocene Thermal Maximum. Paleoceanography 29, 471–488. https://doi.org/10.1002/2014PA002629

Dunkley Jones, T., Lunt, D.J., Schmidt, D.N., Ridgwell, A., Sluijs, A., Valdes, P.J., Maslin, M., 2013. Climate model and proxy data constraints on ocean warming across the Paleocene–Eocene Thermal Maximum. Earth-Science Rev. 125, 123–145. https://doi.org/10.1016/J.EARSCIREV.2013.07.004

Egger, H., Brückl, E., 2006. Gigantic volcanic eruptions and climatic change in the early Eocene. Int. J. Earth Sci. 95, 1065–1070. https://doi.org/10.1007/s00531-006-0085-7

551 Frieling, J., Svensen, H.H., Planke, S., Cramwinckel, M.J., Selnes, H., Sluijs, A., 2016.
552 Thermogenic methane release as a cause for the long duration of the PETM. Proc. Natl.
553 Acad. Sci. 113, 12059–12064. https://doi.org/10.1073/pnas.1603348113

554 Gernon, T.M., Hincks, T.K., Tyrrell, T., Rohling, E.J., Palmer, M.R., 2016. Snowball Earth
555 ocean chemistry driven by extensive ridge volcanism during Rodinia breakup. Nat.
556 Geosci. 9, 242–248. https://doi.org/10.1038/ngeo2632

557 Gutjahr, M., Ridgwell, A., Sexton, P.F., Anagnostou, E., Pearson, P.N., Pälike, H., Norris,
558 R.D., Thomas, E., Foster, G.L., 2017. Very large release of mostly volcanic carbon
559 during the Palaeocene-Eocene Thermal Maximum. Nature 548, 573–577.
560 https://doi.org/10.1038/nature23646

561 Haaland, H.J., Furnes, H., Martinsen, O.J., 2000. Paleogene tuffaceous intervals, Grane Field
562 (Block 25/11), Norwegian North Sea: their depositional, petrographical, geochemical
563 character and regional implications. Mar. Pet. Geol. 17, 101–118.
564 https://doi.org/10.1016/S0264-8172(99)00009-4

565 Haeckel, M., van Beusekom, J., Wiesner, M.G., König, I., 2001. The impact of the 1991
566 Mount Pinatubo tephra fallout on the geochemical environment of the deep-sea
567 sediments in the South China Sea. Earth Planet. Sci. Lett. 193, 151–166.
568 https://doi.org/10.1016/S0012-821X(01)00496-4

569 Hamme, R.C., Webley, P.W., Crawford, W.R., Whitney, F.A., DeGrandpre, M.D., Emerson,
570 S.R., Eriksen, C.C., Giesbrecht, K.E., Gower, J.F.R., Kavanaugh, M.T., Peña, M.A.,
571 Sabine, C.L., Batten, S.D., Coogan, L.A., Grundle, D.S., Lockwood, D., 2010. Volcanic
572 ash fuels anomalous plankton bloom in subarctic northeast Pacific. Geophys. Res. Lett.
573 37, n/a-n/a. https://doi.org/10.1029/2010GL044629

574 Hartnett, H.E., Keil, R.G., Hedges, J.I., Devol, A.H., 1998. Influence of oxygen exposure

time on organic carbon preservation in continental margin sediments. Nature 391, 572–575. https://doi.org/10.1038/35351

Heimdal, T.H., Callegaro, S., Svensen, H.H., Jones, M.T., Pereira, E., Planke, S., 2019. Evidence for magma–evaporite interactions during the emplacement of the Central Atlantic Magmatic Province (CAMP) in Brazil. Earth Planet. Sci. Lett. 506, 476–492. https://doi.org/10.1016/j.epsl.2018.11.018

Hein, J.R., O'Neil, J.R., Jones, O'NEIL, J.R., JONES, M.G., 1979. Origin of authigenic carbonates in sediment from the deep Bering Sea. Sedimentology 26, 681–705. https://doi.org/10.1111/j.1365-3091.1979.tb00937.x

Hembury, D.J., Palmer, M.R., Fones, G.R., Mills, R.A., Marsh, R., Jones, M.T., 2012. Uptake of dissolved oxygen during marine diagenesis of fresh volcanic material. Geochim. Cosmochim. Acta 84, 353–368. https://doi.org/10.1016/J.GCA.2012.01.017

Higgins, J.A., Schrag, D.P., 2006. Beyond methane: Towards a theory for the Paleocene–Eocene Thermal Maximum. Earth Planet. Sci. Lett. 245, 523–537. https://doi.org/10.1016/J.EPSL.2006.03.009

Homoky, W.B., Hembury, D.J., Hepburn, L.E., Mills, R.A., Statham, P.J., Fones, G.R., Palmer, M.R., 2011. Iron and manganese diagenesis in deep sea volcanogenic sediments and the origins of pore water colloids. Geochim. Cosmochim. Acta 75, 5032–5048. https://doi.org/10.1016/J.GCA.2011.06.019

Hong, W.L., Torres, M.E., Kutterolf, S., 2020. Towards a global quantification of volcanogenic aluminosilicate alteration rates through the mass balance of strontium in marine sediments. Chem. Geol. 550, 119743. https://doi.org/10.1016/j.chemgeo.2020.119743

Jones, M.T., Gislason, S.R., 2008. Rapid releases of metal salts and nutrients following the

599 deposition of volcanic ash into aqueous environments. Geochim. Cosmochim. Acta 72,
600 3661–3680. https://doi.org/10.1016/j.gca.2008.05.030

601 Jones, M.T., Percival, L.M.E., Stokke, E.W., Frieling, J., Mather, T.A., Riber, L., Schubert,
602 B.A., Schultz, B., Tegner, C., Planke, S., Svensen, H.H., 2019. Mercury anomalies
603 across the Palaeocene-Eocene Thermal Maximum. Clim. Past 15, 217–236.
604 https://doi.org/10.5194/cp-15-217-2019

605 Kelly, D.C., Nielsen, T.M.J., McCarren, H.K., Zachos, J.C., Röhl, U., 2010. Spatiotemporal
606 patterns of carbonate sedimentation in the South Atlantic: Implications for carbon
607 cycling during the Paleocene-Eocene thermal maximum. Palaeogeogr. Palaeoclimatol.
608 Palaeoecol. 293, 30–40. https://doi.org/10.1016/j.palaeo.2010.04.027

609 Kelly, D.C., Zachos, J.C., Bralower, T.J., Schellenberg, S.A., 2005. Enhanced terrestrial
610 weathering/runoff and surface ocean carbonate production during the recovery stages of
611 the Paleocene-Eocene thermal maximum. Paleoceanography 20, n/a-n/a.
612 https://doi.org/10.1029/2005PA001163

613 Kim, J.-H., Torres, M.E., Haley, B.A., Ryu, J.-S., Park, M.-H., Hong, W.-L., Choi, J., 2016.
614 Marine silicate weathering in the anoxic sediment of the Ulleung Basin: Evidence and
615 consequences. Geochemistry, Geophys. Geosystems 17, 3437–3453.
616 https://doi.org/10.1002/2016GC006356

617 Knox, R.W.O., 1997. The late Paleocene to early Eocene Ash Layers of the Danish Mo-Clay
618 (Fur Formation): stratigraphic and tectonic Significance, in: Thomsen, E., Pedersen,
619 S.A.S. (Eds.), Geology and Palaeontology of the Mo-Clay. Aarhus Geoscience, Aarhus,
620 pp. 7–11. https://doi.org/10.1038/226560a0

621 Komar, N., Zeebe, R.E., 2017. Redox-controlled carbon and phosphorus burial: A
622 mechanism for enhanced organic carbon sequestration during the PETM. Earth Planet.

623 Sci. Lett. 479, 71–82. https://doi.org/10.1016/J.EPSL.2017.09.011

624 Larsen, L.M., Fitton, J.G., Pedersen, A.K., 2003. Paleogene volcanic ash layers in the Danish
625 Basin: compositions and source areas in the North Atlantic Igneous Province. Lithos 71,
626 47–80. https://doi.org/10.1016/J.LITHOS.2003.07.001

627 Littler, K., Röhl, U., Westerhold, T., Zachos, J.C., 2014. A high-resolution benthic stable-
628 isotope record for the South Atlantic: Implications for orbital-scale changes in Late
629 Paleocene-Early Eocene climate and carbon cycling. Earth Planet. Sci. Lett. 401, 18–30.
630 https://doi.org/10.1016/j.epsl.2014.05.054

631 Longman, J., Palmer, M.R., Gernon, T.M., Manners, H.R., 2019. The role of tephra in
632 enhancing organic carbon preservation in marine sediments. Earth-Science Rev. 192,
633 480–490. https://doi.org/10.1016/j.earscirev.2019.03.018

634 Ma, Z., Gray, E., Thomas, E., Murphy, B., Zachos, J., Paytan, A., 2014. Carbon sequestration
635 during the Palaeocene-Eocene Thermal Maximum by an efficient biological pump. Nat.
636 Geosci. 7, 382–388. https://doi.org/10.1038/ngeo2139

637 März, C., Meinhardt, A.K., Schnetger, B., Brumsack, H.J., 2015. Silica diagenesis and
638 benthic fluxes in the Arctic Ocean. Mar. Chem. 171, 1–9.
639 https://doi.org/10.1016/j.marchem.2015.02.003

640 McInerney, F.A., Wing, S.L., 2011. The Paleocene-Eocene Thermal Maximum: A
641 Perturbation of Carbon Cycle, Climate, and Biosphere with Implications for the Future.
642 Annu. Rev. Earth Planet. Sci. 39, 489–516. https://doi.org/10.1146/annurev-earth-
643 040610-133431

644 Morton, A.C., Knox, R.W.O., 1990. Geochemistry of late Palaeocene and early Eocene
645 tephras from the North Sea Basin. J. Geol. Soc. London. 147, 425–437.
646 https://doi.org/10.1144/gsjgs.147.3.0425

Obst, K., Ansorge, J., Matting, S., Hüneke, H., 2015. Early Eocene volcanic ashes on Greifswalder Oie and their depositional environment, with an overview of coeval ash-bearing deposits in northern Germany and Denmark. Int. J. Earth Sci. 104, 2179–2212. https://doi.org/10.1007/s00531-015-1203-1

Pedersen, G.K., Buchardt, B., 1996. The calcareous concretions (cementsten) in the Fur Formation (Paleogene, Denmark): isotopic evidence of early diagenetic growth. Bull. Geol. Soc. Denmark 43, 78–86.

Penman, D.E., Turner, S.K., Sexton, P.F., Norris, R.D., Dickson, A.J., Boulila, S., Ridgwell, A., Zeebe, R.E., Zachos, J.C., Cameron, A., Westerhold, T., Röhl, U., 2016. An abyssal carbonate compensation depth overshoot in the aftermath of the Palaeocene–Eocene Thermal Maximum. Nat. Geosci. 9, 575–580. https://doi.org/10.1038/ngeo2757

Penman, D.E., Zachos, J.C., 2018. New constraints on massive carbon release and recovery processes during the Paleocene-Eocene Thermal Maximum. Environ. Res. Lett 13, 105008. https://doi.org/10.1088/1748-9326/aae285

Planke, S., Rasmussen, T., Rey, S.S., Myklebust, R., 2005. Seismic characteristics and distribution of volcanic intrusions and hydrothermal vent complexes in the Vøring and Møre basins. Geol. Soc. London, Pet. Geol. Conf. Ser. 6, 833–844. https://doi.org/10.1144/0060833

Pohlman, J.W., Kaneko, M., Heuer, V.B., Coffin, R.B., Whiticar, M., 2009. Methane sources and production in the northern Cascadia margin gas hydrate system. Earth Planet. Sci. Lett. 287, 504–512. https://doi.org/10.1016/j.epsl.2009.08.037

Roberts, D.G., Morton, A.C., Backman, J., 1984. Late Paleocene-Eocene volcanic events in the northern North Atlantic Ocean. Initial reports DSDP, Leg 81, Southampt. to Azores 913–923.

671 Sample, J.C., Torres, M.E., Fisher, A., Hong, W.L., Destrigneville, C., Defliese, W.F.,
672 Tripati, A.E., 2017. Geochemical constraints on the temperature and timing of carbonate
673 formation and lithification in the Nankai Trough, NanTroSEIZE transect. Geochim.
674 Cosmochim. Acta 198, 92–114. https://doi.org/10.1016/j.gca.2016.10.013

675 Saunders, A.D., 2016. Two LIPs and two Earth-system crises: The impact of the North
676 Atlantic Igneous Province and the Siberian Traps on the Earth-surface carbon cycle.
677 Geol. Mag. https://doi.org/10.1017/S0016756815000175

678 Schaller, M.F., Fung, M.K., Wright, J.D., Katz, M.E., Kent, D. V., 2016. Impact ejecta at the
679 Paleocene-Eocene boundary. Science (80-.). 354, 225–229.
680 https://doi.org/10.1126/science.aaf5466

681 Scholz, F., Hensen, C., Schmidt, M., Geersen, J., 2013. Submarine weathering of silicate
682 minerals and the extent of pore water freshening at active continental margins. Geochim.
683 Cosmochim. Acta 100, 200–216. https://doi.org/10.1016/j.gca.2012.09.043

684 Schrag, D.P., Higgins, J.A., Macdonald, F.A., Johnston, D.T., 2013. Authigenic carbonate
685 and the history of the global carbon cycle. Science (80-.). 339, 540–3.
686 https://doi.org/10.1126/science.1229578

687 Sivan, O., Schrag, D.P., Murray, R.W., 2007. Rates of methanogenesis and methanotrophy in
688 deep-sea sediments. Geobiology 5, 141–151. https://doi.org/10.1111/j.1472-
689 4669.2007.00098.x

690 Solomon, E.A., Spivack, A.J., Kastner, M., Torres, M.E., Robertson, G., 2014. Gas hydrate
691 distribution and carbon sequestration through coupled microbial methanogenesis and
692 silicate weathering in the Krishna-Godavari Basin, offshore India. Mar. Pet. Geol. 58,
693 233–253. https://doi.org/10.1016/j.marpetgeo.2014.08.020

694 Steinberger, B., Bredow, E., Lebedev, S., Schaeffer, A., Torsvik, T.H., 2018. Widespread

volcanism in the Greenland–North Atlantic region explained by the Iceland plume. Nat. Geosci. 1. https://doi.org/10.1038/s41561-018-0251-0

Stokke, E.W., Jones, M.T., Tierney, J.E., Svensen, H.H., Whiteside, J.H., 2020a. Temperature changes across the Paleocene-Eocene Thermal Maximum – a new high-resolution TEX86 temperature record from the Eastern North Sea Basin. Earth Planet. Sci. Lett. 544, 116388. https://doi.org/10.1016/j.epsl.2020.116388

Stokke, E.W., Liu, E., Jones, M., 2020b. Evidence of explosive hydromagmatic eruptions during the emplacement of the North Atlantic Igneous Province. Volcanica 3, 227–250. https://doi.org/10.30909/vol.03.02.227250

Storey, M., Duncan, R.A., Swisher, C.C., 2007. Paleocene-Eocene thermal maximum and the opening of the Northeast Atlantic. Science (80-.). 316, 587–9. https://doi.org/10.1126/science.1135274

Sun, X., Turchyn, A. V., 2014. Significant contribution of authigenic carbonate to marine carbon burial. Nat. Geosci. 7, 201–204. https://doi.org/10.1038/ngeo2070

Svensen, H., Planke, S., Jamtveit, B., Pedersen, T., 2003. Seep carbonate formation controlled by hydrothermal vent complexes: A case study from the Vøring Basin, the Norwegian Sea. Geo-Marine Lett. 23, 351–358. https://doi.org/10.1007/s00367-003-0141-2

Svensen, H., Planke, S., Malthe-Sørenssen, A., Jamtveit, B., Myklebust, R., Rasmussen Eidem, T., Rey, S.S., 2004. Release of methane from a volcanic basin as a mechanism for initial Eocene global warming. Nature 429, 542–545. https://doi.org/10.1038/nature02566

Torres, M.E., Hong, W.L., Solomon, E.A., Milliken, K., Kim, J.H., Sample, J.C., Teichert, B.M.A., Wallmann, K., 2020. Silicate weathering in anoxic marine sediment as a

719 requirement for authigenic carbonate burial. Earth-Science Rev.
720 https://doi.org/10.1016/j.earscirev.2019.102960

721 Vickers, M.L., Lengger, S.K., Bernasconi, S.M., Thibault, N., Schultz, B.P., Fernandez, A.,
722 Ullmann, C. V., McCormack, P., Bjerrum, C.J., Rasmussen, J.A., Hougård, I.W., Korte,
723 C., 2020. Cold spells in the Nordic Seas during the early Eocene Greenhouse. Nat.
724 Commun. 11. https://doi.org/10.1038/s41467-020-18558-7

725 Wallmann, K., Aloisi, G., Haeckel, M., Obzhirov, A., Pavlova, G., Tishchenko, P., 2006.
726 Kinetics of organic matter degradation, microbial methane generation, and gas hydrate
727 formation in anoxic marine sediments. Geochim. Cosmochim. Acta 70, 3905–3927.
728 https://doi.org/10.1016/j.gca.2006.06.003

729 Wallmann, K., Aloisi, G., Haeckel, M., Tishchenko, P., Pavlova, G., Greinert, J., Kutterolf,
730 S., Eisenhauer, A., 2008. Silicate weathering in anoxic marine sediments. Geochim.
731 Cosmochim. Acta 72, 2895–2918. https://doi.org/10.1016/j.gca.2008.03.026

732 Wallmann, K., Pinero, E., Burwicz, E., Haeckel, M., Hensen, C., Dale, A., Ruepke, L., 2012.
733 The Global Inventory of Methane Hydrate in Marine Sediments: A Theoretical
734 Approach. Energies 5, 2449–2498. https://doi.org/10.3390/en5072449

735 Westerhold, T., Röhl, U., Donner, B., Zachos, J.C., 2018. Global Extent of Early Eocene
736 Hyperthermal Events: A New Pacific Benthic Foraminiferal Isotope Record From
737 Shatsky Rise (ODP Site 1209). Paleoceanogr. Paleoclimatology 33, 626–642.
738 https://doi.org/10.1029/2017PA003306

739 Westerhold, T., Röhl, U., McCarren, H.K., Zachos, J.C., 2009. Latest on the absolute age of
740 the Paleocene–Eocene Thermal Maximum (PETM): New insights from exact
741 stratigraphic position of key ash layers + 19 and − 17. Earth Planet. Sci. Lett. 287, 412–
742 419. https://doi.org/10.1016/J.EPSL.2009.08.027

743 Whiticar, M.J., Faber, E., 1986. Methane oxidation in sediment and water column
744 environments—Isotope evidence. Org. Geochem. 10, 759–768.
745 https://doi.org/10.1016/S0146-6380(86)80013-4

746 5 Figures

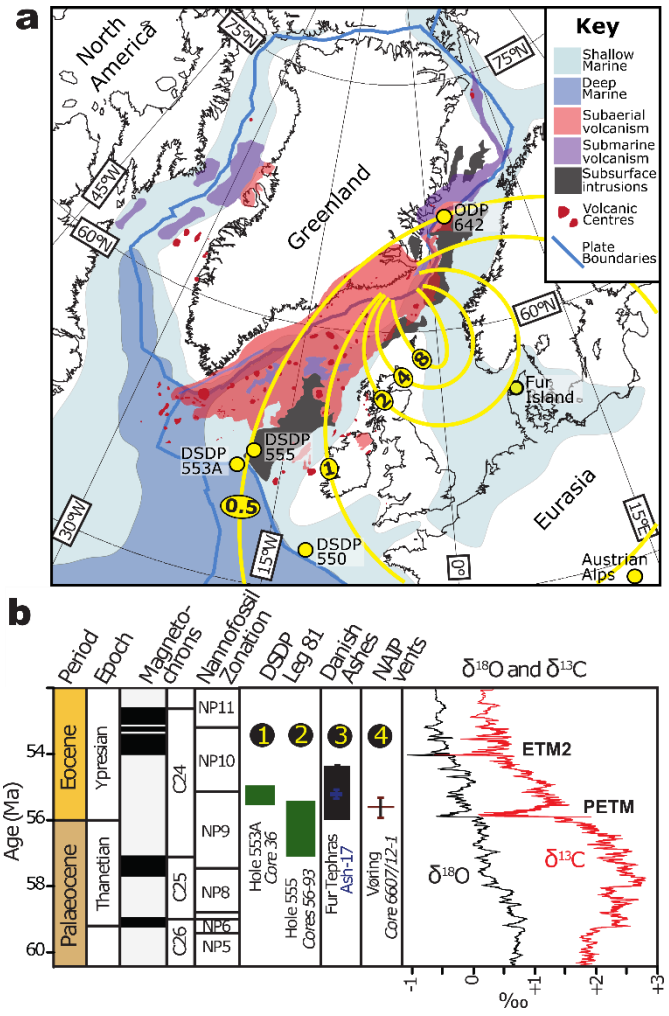

747

748 **Figure 1:** Spatial and temporal distribution of tephras analysed in this study. (a)
749 Palaeogeographic reconstruction of the North Atlantic region at circa 55 Ma displaying an
750 overview of the North Atlantic Igneous Province (NAIP), adapted from Jones et al., (2019).
751 Locations of shallow and deep marine basins are represented by light and dark blue areas,
752 respectively. Locations of extrusive (subaerial and submarine) volcanism are marked in red,
753 with dark red designating discrete volcanic centres. Areas of sill intrusions into sedimentary

basins are shown in dark brown. Note that seismic retrievals below volcanic extrusives are very poor, so the extent of intrusions may be considerable below the red areas shown on the map. Also shown, in yellow, are isopachs of levels of tephra fall (in metres) from explosive volcanism during the period of NAIP activity (taken from Obst et al., (2015)). Locations mentioned in this study are labelled with yellow circles. (b) Indicative age of each of the sections studied, based on nannofossil and magnetostratigraphy, adapted from Stokke et al., (2020b). Also shown is the age of Danish tephras from the Fur formation, and oxygen and carbon isotope curves for the interval (Littler et al., 2014), indicating the excursions that characterise the PETM and other hyperthermal events.

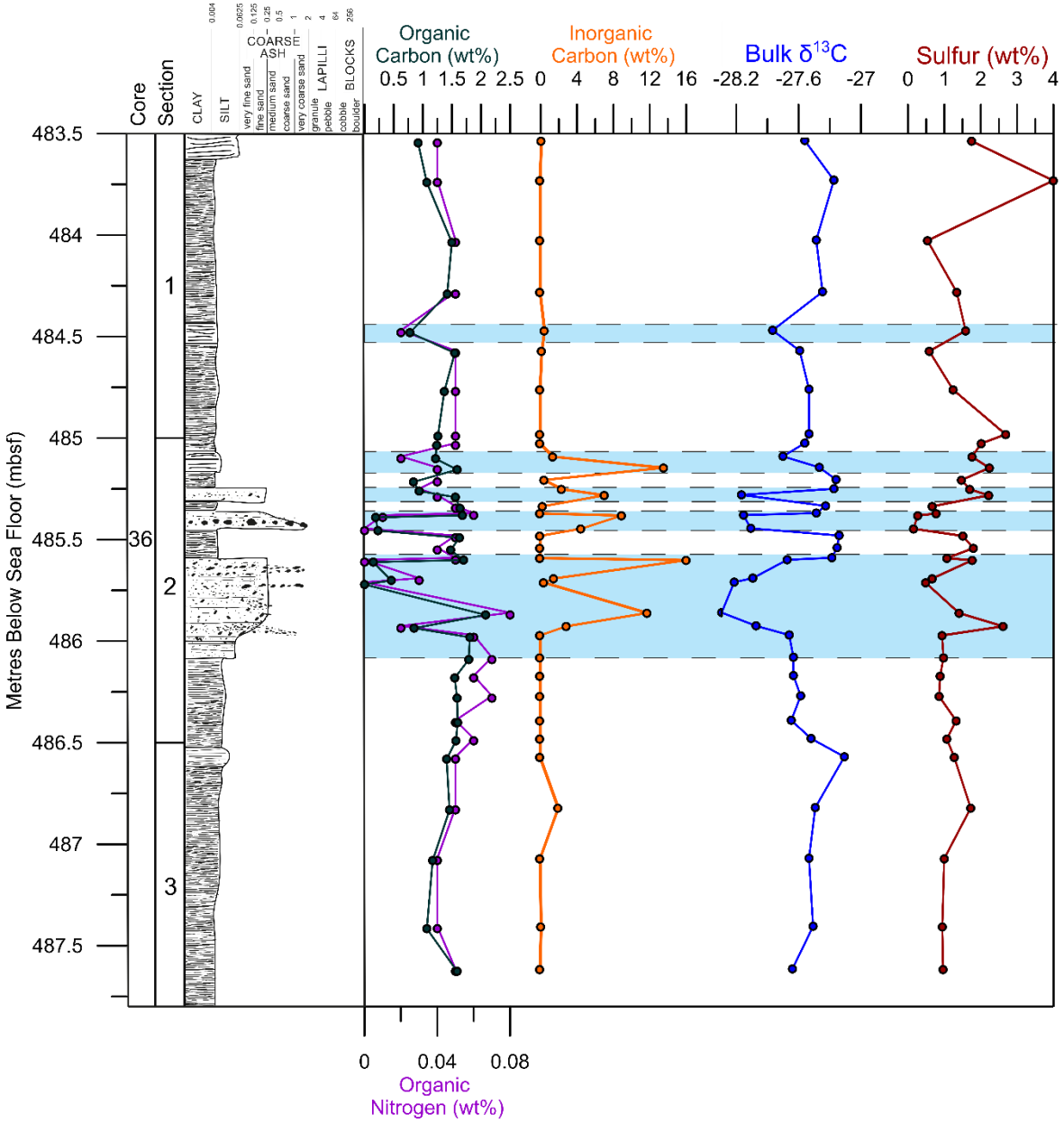

763

764 **Figure 2:** Carbon and sulfur characteristics of tephras and sediments in Hole 553A (Rockall).
765 The downhole graphs show organic carbon, inorganic carbon, organic nitrogen, and sulfur
766 concentrations (in wt%). Also shown is the bulk $\delta^{13}C$ signal, relative to VPDB, and a
767 simplified graphic log of the mudrock and tephra sequence. Tephra layers are highlighted in
768 blue and are consistently enriched in $CaCO_3$ and depleted in organic carbon and $\delta^{13}C$,
769 demonstrating the regular occurrence of carbonate minerals within these layers.

770

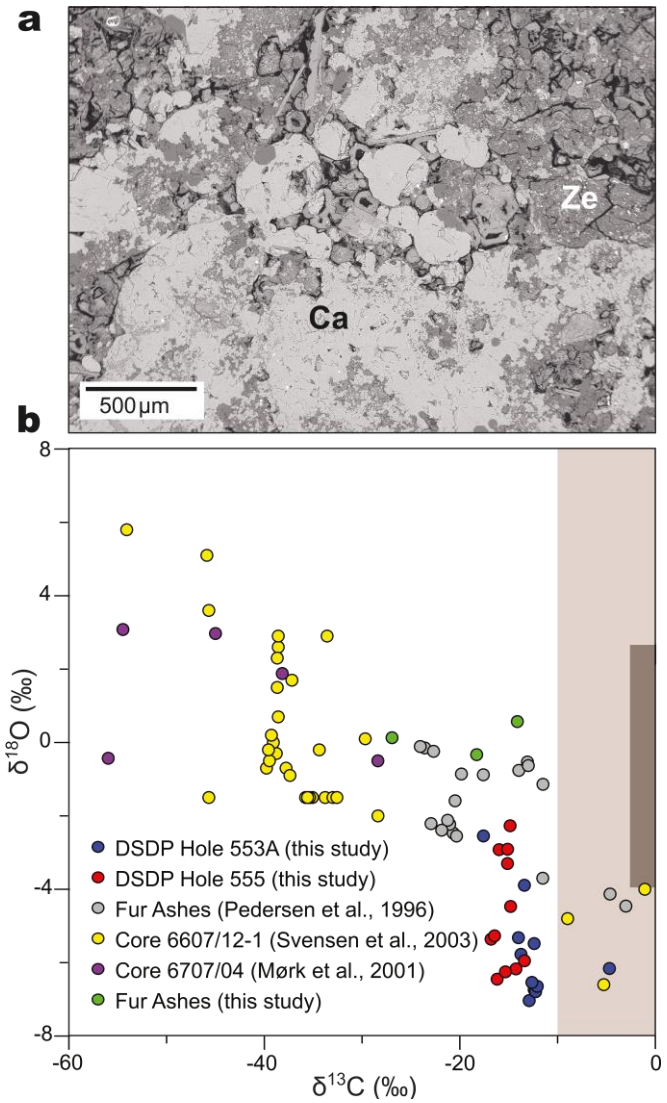

771

772 **Figure 3:** Petrographic and isotopic evidence for the occurrence of authigenic carbonates in
773 the Rockall tephras. (a) SEM image of tephra from the Rockall sequence from Hole 553A
774 (Core 36, Section 2, 86-87cm), with calcite infill (Ca) and zeolite rims (Ze). (b) $\delta^{13}C$ versus
775 $\delta^{18}O$ for the carbonates found within tephras from Hole 553A (blue circles), Hole 555 (red
776 circles) and the Fur formation (green circles). These are presented alongside comparable data
777 from carbonate concretions from PETM-age tephras in Denmark (grey circles), early Eocene
778 ash-hosted carbonates (purple circles) and a hydrothermal vent-hosted carbonate dated to the
779 PETM (yellow circles). Also indicated is the expected signal for seawater (brown rectangle)
780 and primary marine carbonates (shaded grey rectangle). All samples strongly indicate

781 methanogenic processes with a shift toward negative $\delta^{13}C$ values, precluding a biogenic
782 origin for the carbonates.

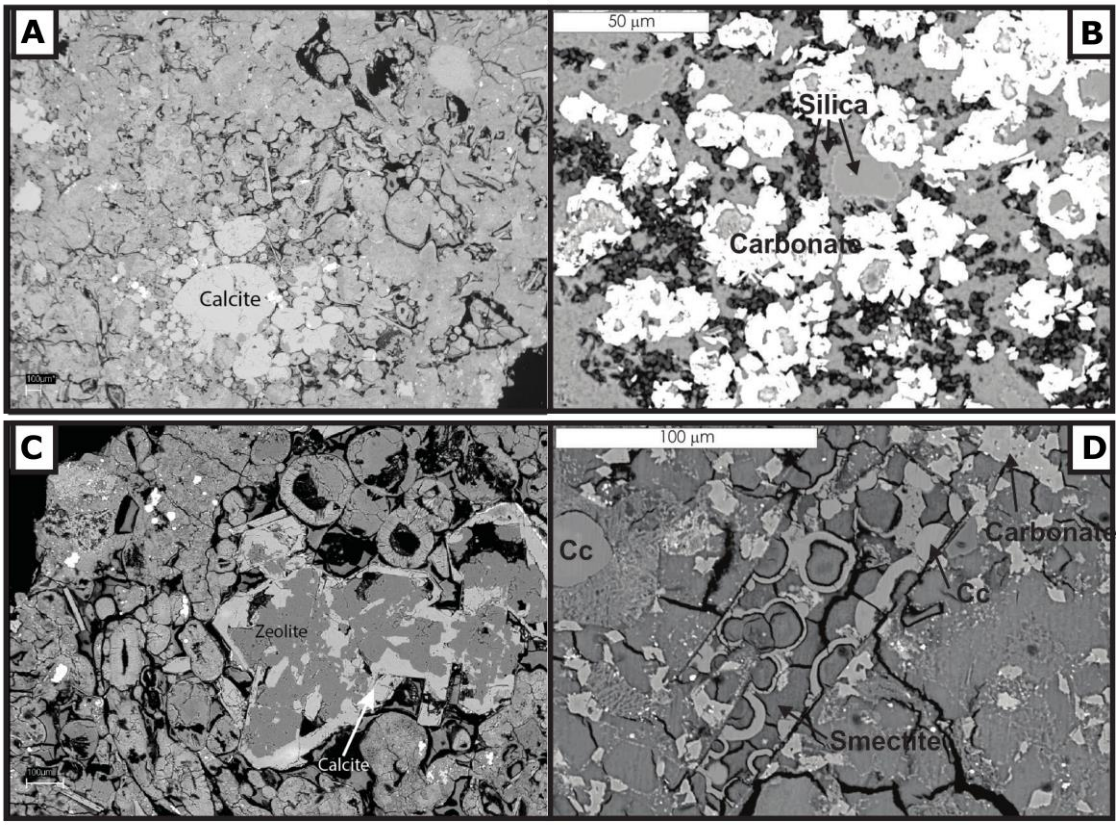

783

784 **Figure 4:** SEM images of authigenic carbonate formation in ash layers. Panels A and C
785 shows tephras from the Rockall sequences, A is from ash layer present in DSDP Hole 553A
786 (Core 36, Section 2, 69-71cm). B is from ash layer present in DSDP Hole 555 (Core 65,
787 Section 1, 105-107cm). Panels B and D shows carbonate infilling as calcite (cc) in samples
788 from core 6607/12-1 from the Vøring Basin.

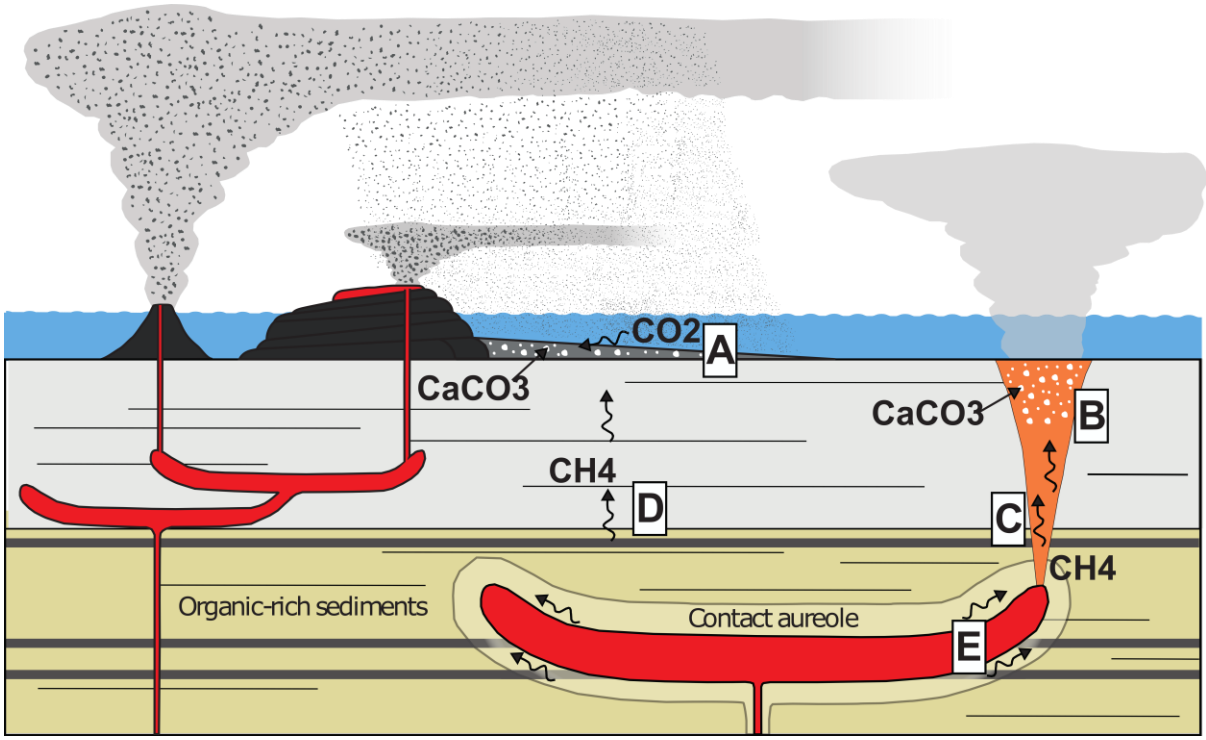

Figure 5: Schematic diagram (not to scale) showing the locations of carbonate formation, and pathways of carbon migration during the PETM. The locations of authigenic carbonate cement formation are (a) in tephra layers and (b) above hydrothermal vent structures. To form these carbonate cements, carbon may be sourced from (c) methane release during hydrothermal vent activity, (d) methane tied to anaerobic oxidation of organic sediments, and (e) methane degassing from contact metamorphism when sills are emplaced in organic-rich sediments. Figure is modified after Heimdal et al., (2019); Jones et al., (2019).

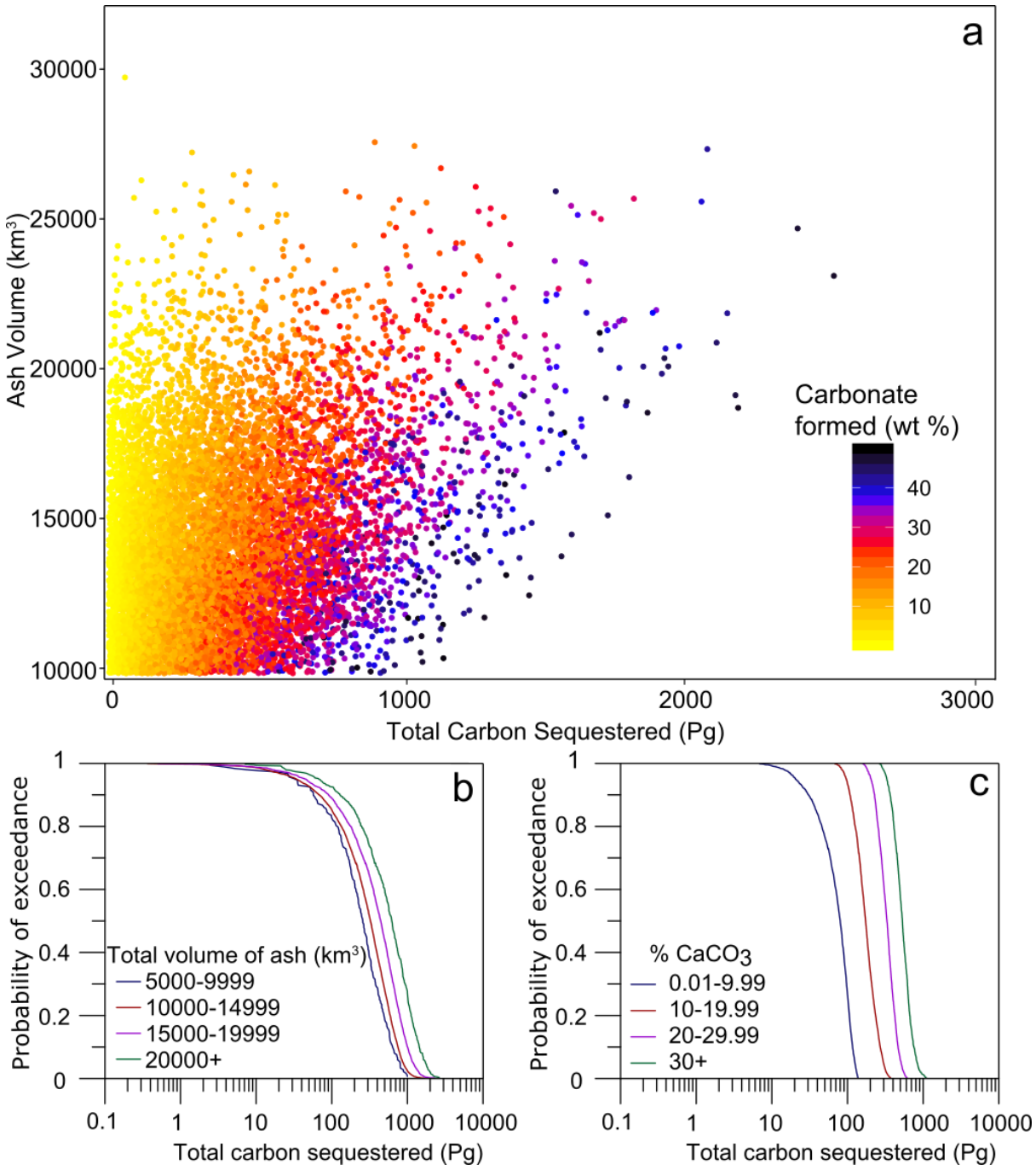

797

798 **Figure 6:** Results of Monte Carlo simulations of carbon sequestration via authigenic
799 carbonate formation in widespread tephra layers. (a) Scatter plot of ash volume versus total
800 carbon sequestered during the PETM, with the amount of carbonate in each model shown in
801 the colour scale bar. (b) Probability of exceedance for models reconstructing a range of
802 eruptive tephra volumes for 9.14% $CaCO_3$, the mean volume measured; (c) Probability of

803 exceedance for models showing tephra-bound $CaCO_3$ content an initial ash volume of 9,691

804 km^3, the output of isopach modelling.

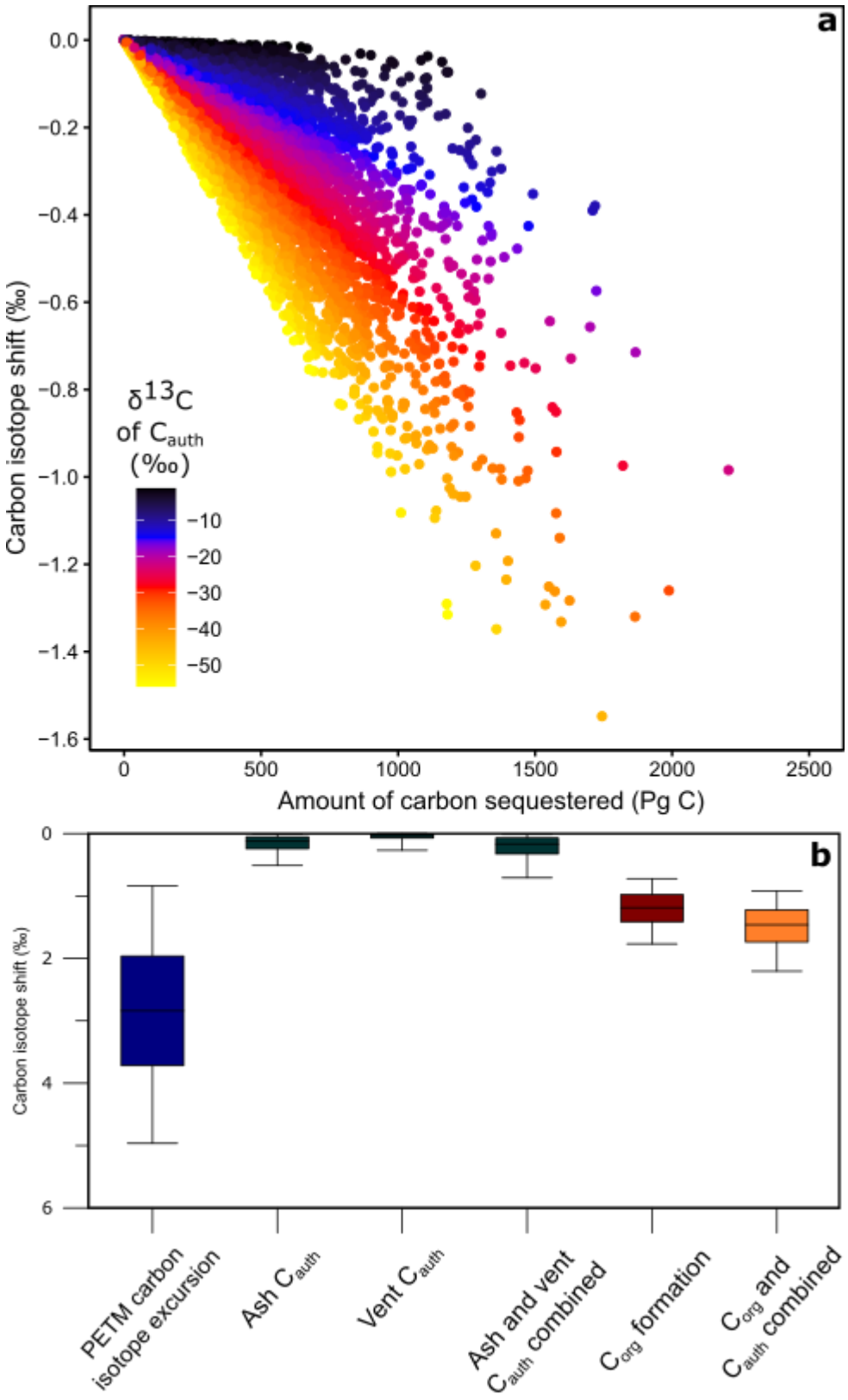

Figure 7: Estimates of the scale of the isotopic shift associated with the sequestration of carbon in authigenic carbonates (C_{auth}) during the PETM. (a) Scatter plot showing the results of Monte Carlo modelling to estimate the impact of C_{auth} sequestration on carbon isotopic

809 composition during the Early Eocene, with the isotopic composition of the sequestered
810 carbon shown in the colour bar. (b) Box and whisker diagrams estimating the magnitude of
811 the isotopic shift associated with the PETM (blue) and the sequestration of carbon in ash and
812 vent C_{auth} (dark green). This shift is compared to the shift associated with enhanced organic
813 carbon (C_{org}; red) burial (see Gutjahr et al., (2017)). Finally, the shift represented by the
814 combination of enhanced C_{org} burial and C_{auth} sequestration due to tephra diagenesis is
815 presented (orange). Boxes are defined by the 25^{th} and 75^{th} percentiles of the data, and
816 whiskers by the 5^{th} and 95^{th} percentiles.

817